Fuel 426 (2026) 139603

Contents lists available at ScienceDirect

Fuel

journal homepage: www.elsevier.com/locate/fuel

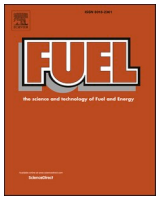

Full Length Article

Limits of high-pressure hydrogen jet combustion in argon power cycle-based energy systems

Iman Chitsaz [a,*], Alireza Kakoee [a], Sajid Ahammed [a], Mahdi Salahi [b], Amin Mahmoudzadeh Andwari [b], Zeeshan Ahmad [c], Jari Hyvönen [c], Maciej Mikulski [a,*]

[a] Efficient Powertrain Solutions, School of Technology and Innovation, University of Vaasa, Wolffintie 34, Vaasa FI-65200, Finland
[b] Machine and Vehicle Design (MVD), Materials and Mechanical Engineering, Faculty of Technology, University of Oulu FI-90014, Oulu, Finland
[c] Wärtsilä Finland Oy, Teollisuuskatu 1, Vaasa FI-65170, Finland

ARTICLE INFO

Keywords:
Argon power cycle
Hydrogen
High-pressure direct injection
Jet ignition
Combustion efficiency
Large-bore engine

ABSTRACT

This study investigates boundaries of ultra-high pressure (300 bar) hydrogen direct injection in a closed-loop argon power cycle, including combustor and working fluid management subsystems. An integrated 1D–3D CFD framework is implemented to assess the effects of key system parameters on combustion phenomenology under real-world operational constraints of a large-bore, medium-speed engine representative of future extrapolated hydrogen power generation systems. The framework is thoroughly validated with experimental data, including measurements of argon-diluted hydrogen jet ignition from a spray-combustion chamber. Simulations confirm that ignition delay is governed by oxygen entrainment and in-cylinder temperature. Three interacting phenomena driving combustion are also identified: rapid premixed burn of residual or entrained hydrogen; mixing-controlled heat release driven by jet momentum and piston interaction; and late-stage decay limited by liner-suppressed momentum loss. The latter phenomenon leads to diffusion flame quenching, which is difficult to overcome through injection calibration or mixture dilution alone. Combustion efficiency above 92% is essential to prevent early-stage pressure rise rates from exceeding the 10 bar/°CA limit, even though recirculated unburned hydrogen has minimal impact (<0.2%) on indicated efficiency. Increasing the injector discharge coefficient or reducing argon/oxygen circuit pressure support more complete combustion, but both measures introduce trade-offs with excessive peak pressure and thermodynamic efficiency respectively. The best observed trade-off at 90% argon and lambda 1.3 is achieved at hydrogen SOI of −20 CA, with moderate discharge and yields thermodynamic efficiency of 51%, below expected targets. The study's flat piston limits mixing during late combustion, so further gains require injector/bowl geometry co-optimisation.

1. Introduction

The expansion of renewables is transforming the energy production paradigm. However, the inherent intermittency and variability of these resources present challenges to grid stability, reliability and dispatchability [1]. Addressing these challenges requires energy storage solutions which decouple supply from demand over time. Among the options, power-to-hydrogen (H_2) has gained attention by converting surplus renewable electricity into H_2 via electrolysis. Proton exchange membrane fuel cells can reconvert H_2 to electricity at efficiencies up to 65% but only at partial load, i.e., at excessive capital and operational cost [2].

Emerging technologies such as the argon power cycle (APC) offer a potentially competitive alternative, combining high efficiency with compactness and the ability to valorise electrolysis off-streams [3,4]. By replacing air with argon (Ar), the APC improves thermal efficiency and eliminates NO_x formation [5]. However, its practical implementation remains challenged by real-world operational constraints, particularly related to closed-loop operation, argon recirculation, and off-stream integration. As a result, the technology is still at a low maturity level.

Significant progress in APC technology has been made using hydrocarbon fuels [6]. Aznar et al. [7,8], demonstrated that direct-injection compression ignition (CI) outperforms port-injection spark ignition (SI), offering higher efficiency and extended operating range by mitigating knock. APC in homogeneous charge compression ignition (HCCI) mode with *iso*-octane [9,10] and natural gas [11], has consistently shown efficiency gains of up to 30% over air cycles. However, the

* Corresponding authors.
E-mail addresses: iman.chitsaz@uwasa.fi (I. Chitsaz), maciej.mikulski@uwasa.fi (M. Mikulski).

https://doi.org/10.1016/j.fuel.2026.139603
Received 27 January 2026; Received in revised form 13 April 2026; Accepted 20 April 2026
Available online 25 April 2026

Nomenclature

Abbreviations

A	area [m^2]
APC	argon power cycle
ATDC	after top dead centre [^oCA]
BTDC	before top dead centre [^oCA]
CA	crank angle
CA10	crank angle that 10% of fuel is burned
CA50	crank angle that 50% of fuel is burned
CFD	computational fluid dynamics
CI	compression ignition
C_d	discharge coefficient
CR	compression ratio
EVO	exhaust valve open
HRR	heat release rate [$J/^oCA$]
IHR	integrated heat release rate [J]
IMEP	indicated mean effective pressure [bar]
IVC	intake valve close
IVO	intake valve open
$\dot{m}$	mass flow rate [kg/s]
M	Mach number
P	pressure [pa]
PRR	pressure rise rate [bar $/^oCA$]
R	gas constant [J/ $kg.K$]
RMSE	root mean square error
SI	spark ignition
SOC	start of combustion [^oCA]
SOI	start of injection [^oCA]
t	time scale [s]
T	temperature [K]
TDC	top dead centre
TKE	turbulent kinetic energy [m^2/s^2]

Greek Letters

α	thermal diffusivity [m^2/s]
ε	turbulent kinetic energy dissipation rate
η_c	combustion efficiency
η_i	engine indicated efficiency
δ_t	thermal boundary layer thickness[m]
λ	ratio of actual oxygen-fuel ratio to the stoichiometric
γ	specific heat ratio

practical use of these fuels in closed-cycle APC is limited by challenges in CO_2 removal and storage [8].

Initial research into APC with H_2 was conducted by Cornell University [12] and Kyoto University [13], followed by experimental validation by Toyota Motor Corporation, which employed SI architecture and achieved efficiencies of up to 41% [14]. Killingsworth et al. [15] investigated the effect of compression ratio(CR), finding that knock limited CR to 4.5:1, with a peak thermal efficiency of 44%.

Tongji University initiated consistent experimental investigations into SI H_2–APC in 2017 [16,17] with contemporary single-cylinder research engine architecture. Recent works by Jin et al. [18] and Ding et al. [19] investigated knock suppression via water injection, achieving a net thermal efficiency of 52.41% at a CR of 9.6:1. Their subsequent research extended to include Miller cycle [20], methane addition [21] and charge stratification [22]. All these were aimed at suppressing H_2 pre-ignition and thermal loading, identified as the main showstopper for maximising efficiency. Recently, WTZ [23,24] announced a closed loop H_2-APC implementation with Ar recovery, claiming a peak thermal efficiency of 55%. However, available data suggest this figure was achieved under partial load, with limited technical details disclosed.

On the other hand, compression ignition (CI) of H_2 in APC seems more futuristic than spark ignition due to the knock-free operation. Mat Taib et al. [25–27] employed CFD to investigate H_2 CI in noble gas environments, using the baseline geometry of a heavy-duty Yanmar NF19SK diesel engine. Their work focused primarily on comparing working fluids, highlighting helium's superior thermophysical properties over Ar. However, the studies assumed an injection pressure of only 80 bar, limiting the analysis to low-load conditions and excluding practical constraints such as durability and thermal limits. Van den Brink [28] used CFD to simulate combustion phenomena in a jet ignition Ar-O_2(Ar-H_2) environment. The study revealed that direct H_2 injection gave better thermal performance than O_2 injection, due to mitigated heat losses.

The energy industry has recently shown significant interest in H_2-APC [29,30], while most studies remain highly idealised, focused on premixed conditions, generic geometries or simulations detached from real engine constraints. In particular, H_2 jet ignition under argon dilution has only been superficially addressed, typically through fundamental experiments lacking practical constraints such as permissible pressure, temperature and combustion efficiency on the combustor, not to mention the system level. Consequently, key limitations arising from jet dynamics, ignition delay and incomplete combustion remain unresolved in the context of the intended application.

While previously reported indicated engine efficiencies range from 44% to 60%, the present study aims to evaluate the maximum attainable efficiency by systematically varying independent engine parameters. This work also addresses that gap by conducting the first comprehensive numerical investigation of H_2 high-pressure direct injection in a full closed-loop APC engine. Unlike previous studies, the simulations are performed using a high-fidelity CFD–1D coupled framework, validated across both combustion and system-level performance, and applied to architecture reflecting the intended application in stationary power generation.

In this study, flat piston is selected to be studied to remove geometry-induced effects, providing a controlled framework to study the fundamental behaviour of hydrogen jet ignition and combustion in an Ar–O_2 environment. Under these conditions, the study clarifies the underlying combustion phenomenology while demonstrating the fuel's inherent capability for efficient mixing and energy release without geometric assistance and uses these insights to guide hardware design and calibration strategies for full-scale APC implementation.

2. Methods

In this study, a prototype APC combustor based on Wärtsilä 20 cylinder geometry, is investigated. The core simulations are conducted using Converge Studio CFD package. The whole APC is simulated using 1-dimentional (1D) GT-Suite, including charge cooler and condenser for combustion products (H_2O) recovery. The 1D solution establishes boundary conditions for CFD simulation, including cylinder scavenging and combustion.

The simulation framework is explained in Fig. 1. Note that, for each iteration, the CFD-predicted burn rate is re-imposed to the 1D model, which in turn feeds the intake manifold mixture conditions and predicted cylinder-wall temperatures as boundary conditions for the CFD solver. Co-simulation is run until the changes in solid wall temperature and heat release rate (HRR) do not exceed 5 K and 3% respectively. The routine ensures simulations are robustly linked to real engine conditions.

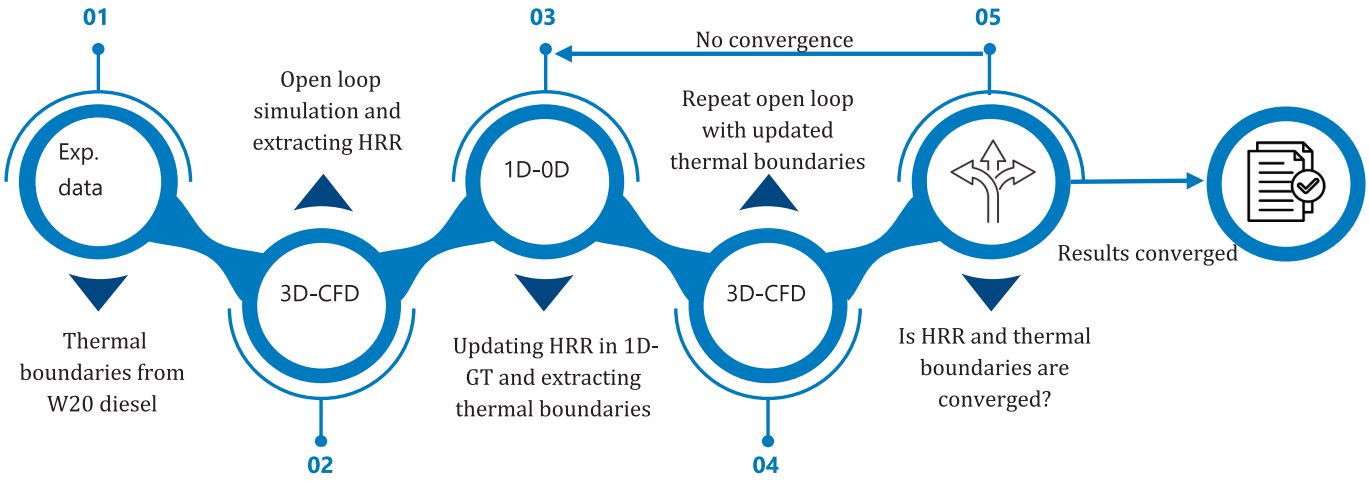

Fig. 1. Schematic of the simulation process including 3D converge studio and 1D GT-Suite.

2.1. The research object and its representative GT-Suite model

The key specifications of the investigated single-cylinder research engine are summarized in Table 1. Its principal geometrical parameters are consistent with the production engine, but a flat-crown piston was intentionally adopted. This simplification aligns with the study's objectives, enabling the decoupling of the effects of governing control parameters on H_2 jet combustion in an APC engine from those associated with detailed geometric features.

The corresponding 1D-model of the base engine is provided by the engine manufacturer (Wärtsilä),including well-calibrated airpath and cylinder components, with valve flow coefficients established from dedicated flow-bench tests. The baseline GT-Power model further includes a finite-element-method-based wall thermal solver. This predictive methodology is essential for realistic estimation of wall temperatures in the absence of experimental data on heat transfer in APC conditions. Details of the methodology and its calibration for a sister Wärtsilä "MONO" engine, one can find in the recent work of Kakoee et. al. [31].

The validated baseline model is consecutively adapted to represent closed-loop operation in APC with H_2. The adaptation process is thoroughly discussed in the work by Ahammed et al. [32], which further provided results for detailed design of the planned APC plant. The APC system model, corresponding to the mentioned detail design, used in the present simulation framework, is illustrated in Fig. 2.

Relevant changes compared to its referenced predecessor [32], include a more detailed semi-predictive condenser and heat-exchanger models calibrated to real performance data. Other detailed changes include the geometries of the pipe layout and pulsation-reducing buffer tanks, as evident from Fig. 2. Final differences include changing the fuel control logics to accommodate direct H_2 injection and the explored combustion concept. The simulations are run with coolant and lube oil circuit temperature fixed to 85 °C, regardless of the load point.

Table 1
Specifications of the Wärtsilä 20 single-cylinder research engine.

Engine Specification	Value
Bore	200 mm
Stroke	280 mm
Connecting rod length	510 mm
Crank offset	0 mm
Valvetrain	four valves per cylinder
Intake valve timing	−373 to −231 CA ATDC
Exhaust valve timing	−580 to-342 CA ATDC
Number of injector nozzles	9
Umbrella angle	140
Piston crown shape	flat

2.2. CFD computational framework

2.2.1. Computational domain and mesh structure

Fig. 3 illustrates the computational domain, which includes the intake and exhaust runners and a moving piston interface. The meshing further involves the cylinder head with moving valves, along with the centrally mounted, high-pressure H_2 injector (Fig. 3, right-hand side). The injector nozzles are defined as the inlet boundary condition, supplying pure H_2.

The present study performed a mesh sensitivity analysis to assess the mesh structure in terms of computational time and accuracy, evaluating eight different structures for one of the simulation cases.

Table 2 presents the eight different mesh structures investigated. The adaptive mesh refinement levels for velocity, density, and species are set to 2 for all cases. Additionally, a mesh embedding level of 3 is applied around the intake and exhaust valves to improve the accuracy of valve motion modelling. Due to the presence of under-expanded jets resulting from H_2 injection, a conical cylinder with a mesh embedding level of 5 is defined around each injector nozzle to capture the flow characteristics more accurately.

2.2.2. Relevant modelling assumptions

The present study investigates the auto-ignition behaviour of H_2 under CI conditions, where accurate modelling of H_2 combustion is essential. Based on prior research, the SAGE combustion solver, coupled with the C3 hydrogen combustion mechanism [33], is employed to simulate the combustion process in an argon-diluted environment. This mechanism comprises 37 reactions involving 12 species and six chemical elements. Combustion is modelled from the SOI to the end of the engine cycle. The k-ε turbulence model is used to represent turbulent flow behaviour, and the Redlich–Kwong equation of state is applied for simulating compressible gas dynamics. The turbulence model and its parametrisation is adopted from the earlier CFD simulation study by Kakoee et al. [34], concerning similar W20 cylinder geometry. The present study implements effective averaged diffusion coefficients to model binary diffusion coefficients because of their accuracy and lower computational cost [35]. This simplification neglects cross-diffusion effects and differential diffusion driven by multicomponent interactions. In an Argon-rich environment, this approximation may introduce additional uncertainty due to the large molecular weight and low diffusivity of Argon compared to lighter species such as H_2. In particular, the presence of Argon can enhance differential diffusion effects and modify species transport rates, which are not fully captured by the mixture-averaged approach.

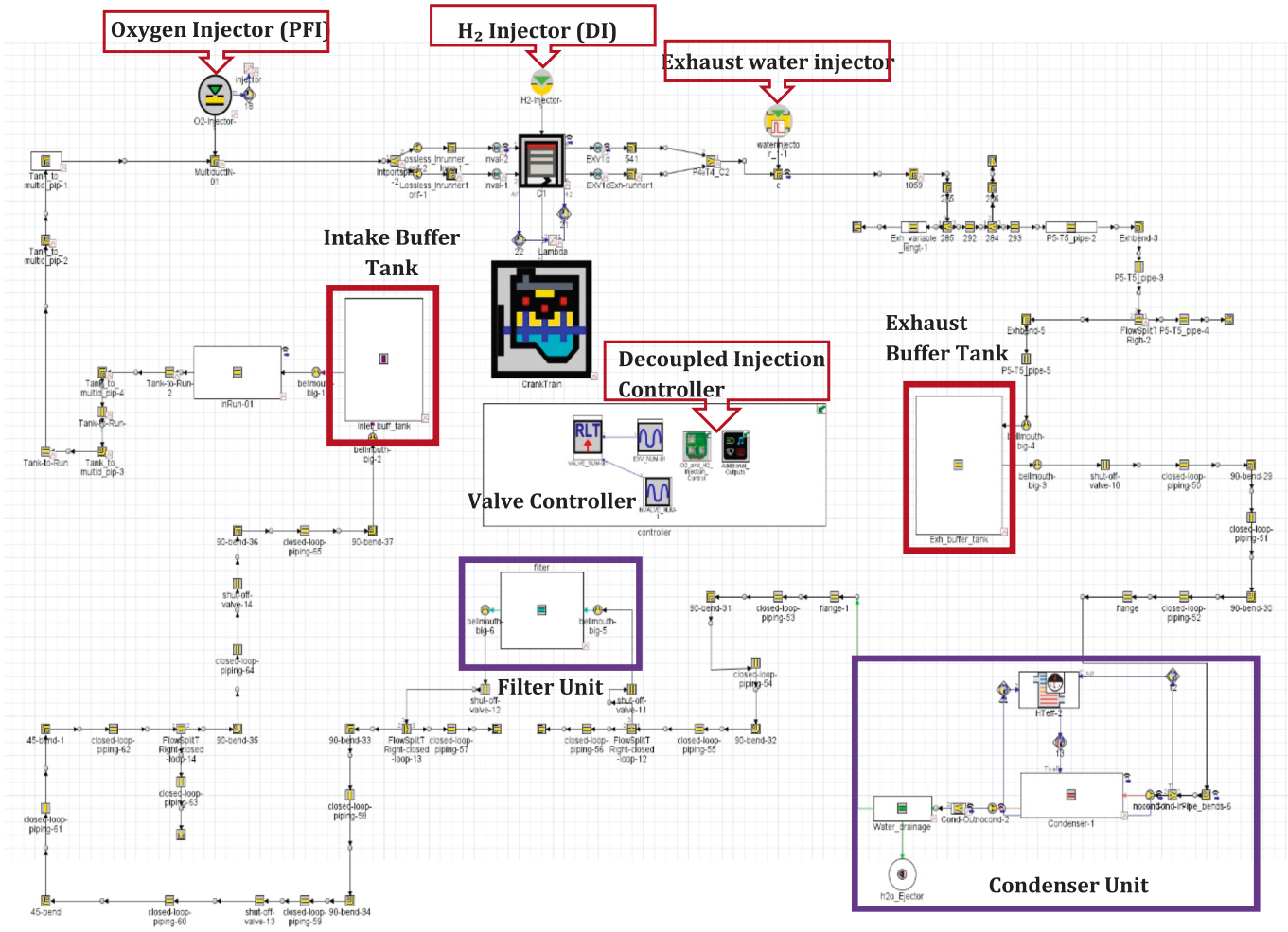

Fig. 2. Schematic of the closed-loop H_2 APC model built in GT-Suite software.

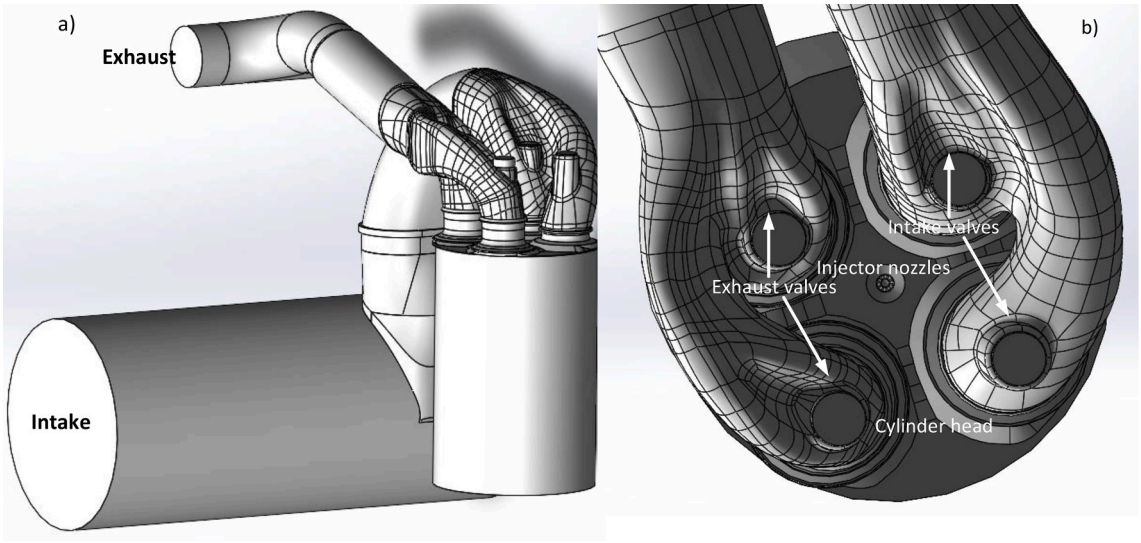

Fig. 3. The computational domain of the W20 single-cylinder research engine: a) whole geometry including intake and exhaust, b) valves and injector nozzles in cylinder head.

However, previous studies [27] have shown that mixture-averaged diffusion provides a reasonable approximation for global combustion characteristics, especially when the flow is dominated by convection and large-scale mixing. In the present configuration, the good agreement observed in early-time temperature and HRR evolution suggests that the impact of this simplification remains limited for the primary phenomena

Table 2
Different mesh structures investigated for mesh dependency study, with variations highlighted in bold.

	Mesh 1	Mesh 2	Mesh 3	Mesh 4	Mesh 5	Mesh 6	Mesh 7	Mesh 8
Base size	6 mm	4 mm	4 mm	5 mm	4mm	5 mm	5 mm	4 mm
Cylinder embeding	1	1	2	2 after SOI	2 after SOI	−25 to −20 CA	2 after SOI	2 after SOI
Adaptive mesh refinement for T	2	2	2	3	3	4	4	4

of interest. Table 3 summarises the submodels and their governing parameters.

H_2 is injected through nine individual nozzle orifices, which are implemented as inlet boundary conditions. The mass flow rates are estimated via a standard isentropic flow correlation with choked flow condition [36]. As reported in previous experimental studies [37–39], the mass flow profile of high-pressure gas injection typically follows a near-trapezoidal shape, characterised by a rapid rise in flow rate (approximately 1.5° CA at 1000 rpm [39]), a quasi-steady phase and a sharp decline(1.5° CA at 1000 rpm).

2.3. Model validation methodology

The validity of the 1D airpath model and connected thermal solver for baseline geometry has been experimentally verified in the previous studies [31], and so is not discussed here in detail. To ensure the credibility of the developed CFD framework, the numerical model is validated against two independent experimental datasets, covering both mixture formation and combustion characteristics. Validation of the H_2 jet development and mixing process uses experimental data from the Sandia National Laboratories optical hydrogen engine [37]. Its H_2 injection is admitted via a single-hole injector at the pressure of 100 bar. The postprocessed H_2 mole fraction that is extracted from planar laser-induced fluorescence (PLIF) is used and compared with simulation results using the same geometry.

Due to the lack of engine experiments, the present simulation's combustion phase is validated using H_2 jet ignition in Ar-O_2 environment, investigated by Mansor and Shioji [40]. Fig. 4 depicts their geometry, used to validate the present simulation. The same injection strategy (trapezoidal mass-flow profile) and mesh resolution in the current simulations are applied for both validation paths.

2.4. Design of simulations and postprocessing methods

Table 4 summarises the investigative simulation campaigns, with each campaign linked to the corresponding results section. The CR is extracted, based on 1D-optimised APC operating condition at 21.5 bar IMEP, corresponding to approximately 75% load of the baseline Wärtsilä 20 engine, as established in previous thermodynamic studies by Ahamed et al. [32]. The scope of this investigation includes: (i) the effects of direct H_2 injection (timing and flow coefficient); (ii) cross-cycle coupling

Table 3
Summary of submodels used in the CFD simulations.

Submodel type	Approach	Reference	Notes / parameters
Combustion/ chemistry	SAGE solver + C3 H_2 mechanism	Dong et al. [33]	37 reactions, 12 species;
Turbulence	Standard k–ε model	Kakoee et al. [3445]	.
Diffusion	Mixture averaged diffusion coefficients	Turns [35]	Effective averaged binary diffusion coefficients
Gas dynamics	Redlich–Kwong	Wang et al. [46]	
Turbulence–chemistry interaction	Direct coupling	–	No presumed PDF model

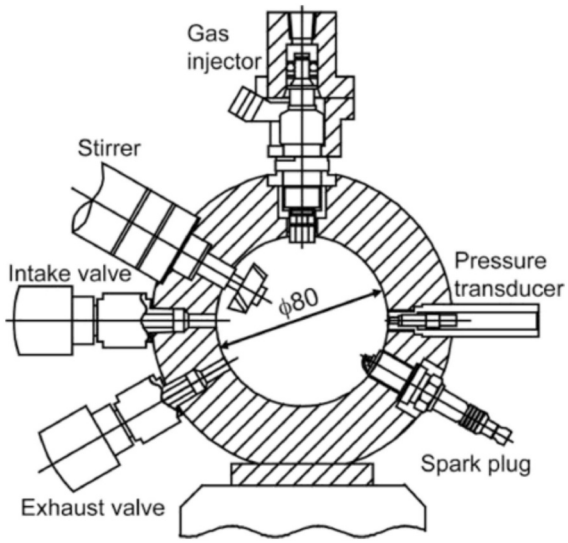

Fig. 4. Schematic of experimental set up for H_2 jet ignition validation validation in argon-oxygen environment reproduced from Mansor et al. [40] with permission from Elsevier.

Table 4
Operating and boundary conditions for different parts of results section: bolded quantities indicate a change vs. previous campaign.

	Sections 3.1 and 3.3	Section 3.4	Section 3.5	Section 3.6
Campaign	Reference case	Injection parameters	Effect of premixed H_2	Mixture parameters
λ	1.1	1.1	1.1	**variable**
SOI	−15° CA ATDC	**variable**	variable	**−20° CA ATDC**
Discharge coef. (Cd)	0.8	**variable**	**0.8**	**0.6**
Ar rate	90%	90%	90%	**85% to 95%**
Exhaust temperature	885 K	**case dependent**	**case dependent**	**case dependent**
H_2 injected mass	382 mg	382 mg	**352 mg**	**382 mg**
Intake pressure	3.7 bar	3.7 bar	3.7 bar	**variable**
Exhaust pressure	4 bar	4 bar	4 bar	**variable**
CR	12:1	12:1	12:1	12:1
Injection pressure	300 bar	300 bar	300 bar	300 bar
Injection temperature	300 K	300 K	300 K	300 K
Intake temperature	321 K	321 K	321 K	321 K
Engine speed	1000 rpm	1000 rpm	1000 rpm	1000 rpm

phenomena involving residual unburned H_2 and its influence on subsequent combustion; and (iii) the impact of mixture parameters on APC combustion performance.

Table 4s CFD simulations begin at −390° CA ATDC, during the late exhaust stroke, and conclude at 330° CA ATDC. This captures the full gas exchange process, including turbulence generation from valve motion

and its subsequent dissipation after intake valve closure (IVC).

The gross heat release rate (HRR) is post-processed from the simulated pressure and temperature trace, using standard first-law analysis, considering instantaneous (chemical) mixture specific heats and corrected to the "gross" reference by considering the heat transfer losses. Combustion phasing indicators (CA10, CA50 and CA90) are further calculated by referencing the gross integrated heat release (IHR) to the CA of 10%, 50%, and 90% of the total released energy. The start of combustion (SOC) is identified by a sharp increase in HRR (50 J/CA threshold), with ignition delay considered as CA between SOI and SOC [38].

Consequently, the net indicated efficiency (including gas exchange losses) is evaluated using a modified metric which accounts only for the chemical energy released from the burned portion of the fuel. The contribution of unburned fuel is excluded, as it is assumed to be fully combusted in the subsequent closed-loop cycle. The combustion efficiency is separately monitored per simulation cycle.

3. Results

3.1. Mesh sensitivity study on target geometry

Fig. 5 illustrates the in-cylinder temperature and HRR for the different mesh configurations. The simulation results before the SOI and SOC are largely consistent across all mesh structures, indicating minimal sensitivity in this phase. Consequently, mesh refinements are primarily concentrated after the SOI, where increased sensitivity to flow dynamics and combustion processes is expected.

Table 5 gives the number of mesh cells at top dead centre(TDC) for each mesh structure, along with the corresponding combustion phasing and computational time (from IVC to EVO). Notably, the results for the last two mesh configurations (Mesh 7 and Mesh 8) converge with differences of less than 2%. The computational cost, however, increases significantly for Mesh 8, so Mesh 7 is selected as the optimal configuration for the remaining simulations due to its balance between accuracy and computational efficiency.

3.2. Injection/combustion model validation

Validation of the CFD model regarding H_2 diffusion and mixing uses experimental data from Sandia's optical H_2 engine [37], reproduced via the same mesh strategy and trapezoidal profile that is used in the current study. Fig. 6 compares the results for different CAs, showing good agreement with the experimental data.

Fig. 7 illustrates validation of the simulated jet-ignition combustion process within the current CFD framework, comparing it with results from previous experiments on H_2 jet ignition in an Ar–O_2 environment by Mansor et al [39,40]. The experimental case corresponds to an argon mass fraction of 90% and an initial chamber temperature of 1,100 K, which is most comparable to the combustion conditions of the present study. H_2 is injected into initially pressurised (4 MPa) chamber, at 8 MPa through a 0.8 mm nozzle. Note, that the modelled geometry excludes the stirrer and spark plug, due to insufficient geometrical data related to these objects.

Fig. 7a shows that the model accurately predicts experimental chamber temperature histories, with a normalised RMSE below 2.5%. As shown in Fig. 7b the deviation in HRR between approximately 5 and 10 ms corresponds to the phase when the propagating flame front reaches the region occupied by the mechanical stirrer in the experiments. It is important to note that the stirrer is only operated prior to injection to ensure mixture homogeneity and does not rotate during the combustion event. Therefore, its influence on the flow is not through sustained turbulence generation, but rather through its role as a solid obstruction within the chamber.

The presence of the stirrer effectively increases the surface area available for heat transfer and promotes flame quenching through wall interactions. As the flame impinges on the stirrer, local heat losses and radical recombination at the surface reduce the reaction rate, leading to the observed drop in HRR in the experiments. In contrast, the CFD model does not include this internal geometry, and therefore does not capture these wall-induced quenching effects, resulting in a more sustained heat release rate during this phase.

The good agreement observed during the initial 0–5 ms period supports this interpretation, as the flame development in this interval is dominated by jet evolution and large-scale mixing processes, with negligible interaction with the stirrer. Consequently, the discrepancies at later times can be attributed primarily to the absence of solid-surface-induced quenching rather than inaccuracies in the predicted mixing or combustion behaviour.

3.3. Phenomenological aspects of H_2 jet ignition in argon atmosphere

Fig. 8 shows the in-cylinder turbulent kinetic energy (TKE) and epsilon(ε) as a function of CA, along with key valve-timing events. Fig. 8a highlights that peak TKE occurs as the intake valve closes, following its maximum lift. This indicates that the interaction between the intake valve flow and the cylinder volume during the closing phase generates the highest turbulence intensity.

While TKE and ε generally follow similar trends, the maximum ε is observed at the point of maximum intake valve lift, rather than during the closing period. This distinction suggests that ε, which represents the rate at which turbulent energy dissipates into heat, is more closely associated with the high shear regions formed at peak valve lift. Notably, Fig. 8b shows the results of in-cylinder trapped mass from the CFD and

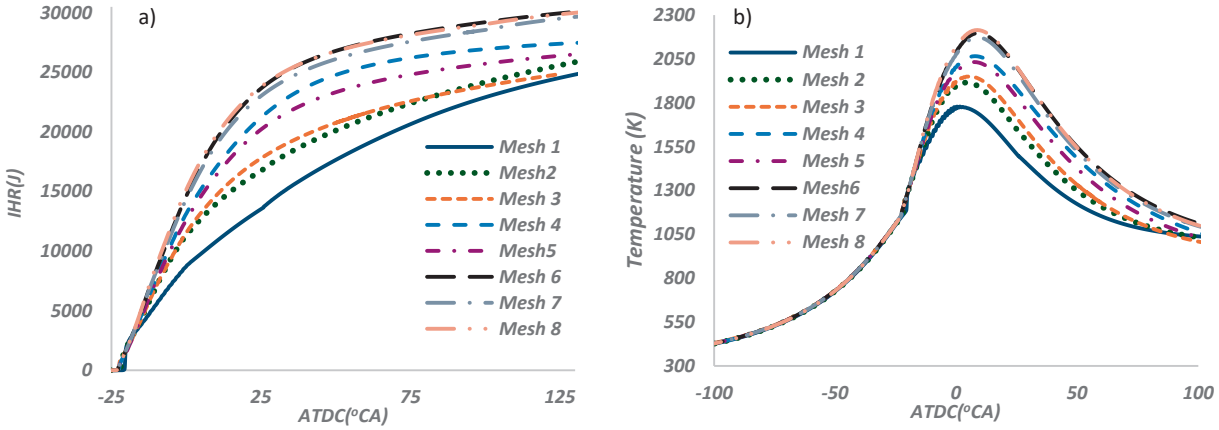

Fig. 5. Mesh sensitivity analysis based on W20 geometry: a) Integrated HRR profiles, b) In-cylinder temperature.

Table 5
Combustion phasing results and runtime for different mesh configurations.

	Mesh 1	Mesh 2	Mesh 3	Mesh 4	Mesh 5	Mesh 6	Mesh 7	Mesh 8
CA10	−16	−16	−16	−16	−17	−17	−17	−17
CA50	47	28	22	13	11	6	5	4
Cell counts @ TDC(million)	0.42	1.4	1.5	2	5.2	7.3	7.5	10
Closed-loop runtime(hour)	12	54	68	25	107	146	150	229

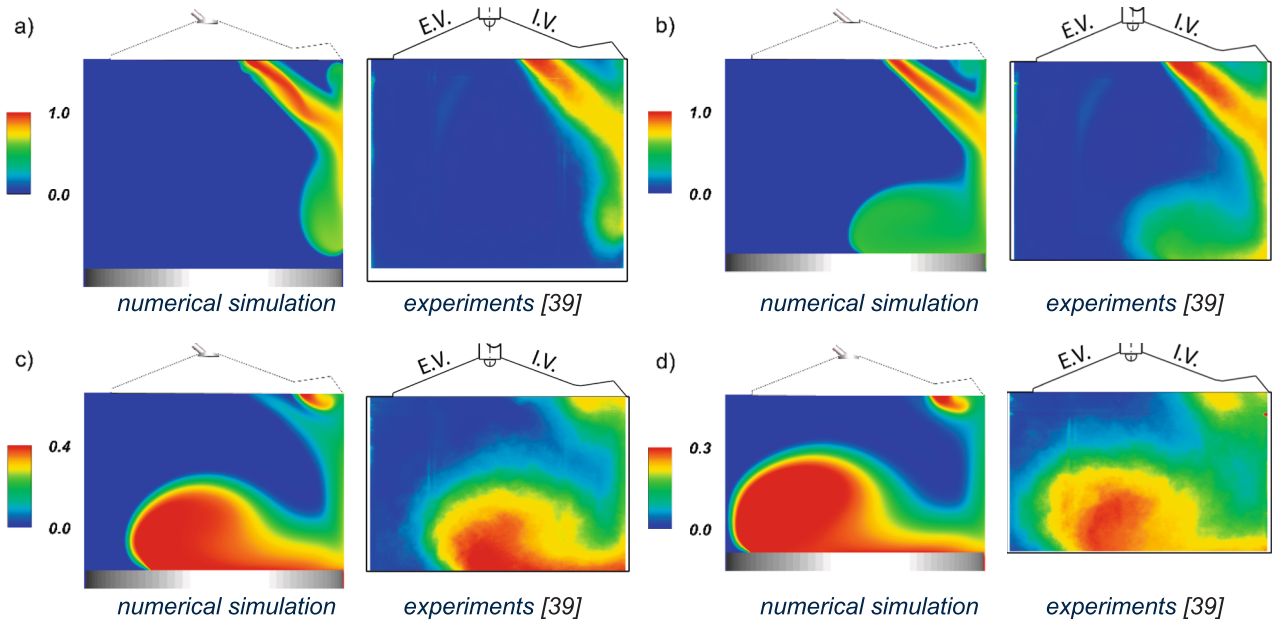

Fig. 6. Comparison of H_2 mole fraction distribution of numerical and experimental results (adapted based on data from Sandia [37]): a) −130° CA ATDC, b) −120° CA ATDC, c) −110° CA ATDC, d) −100° CA ATDC.

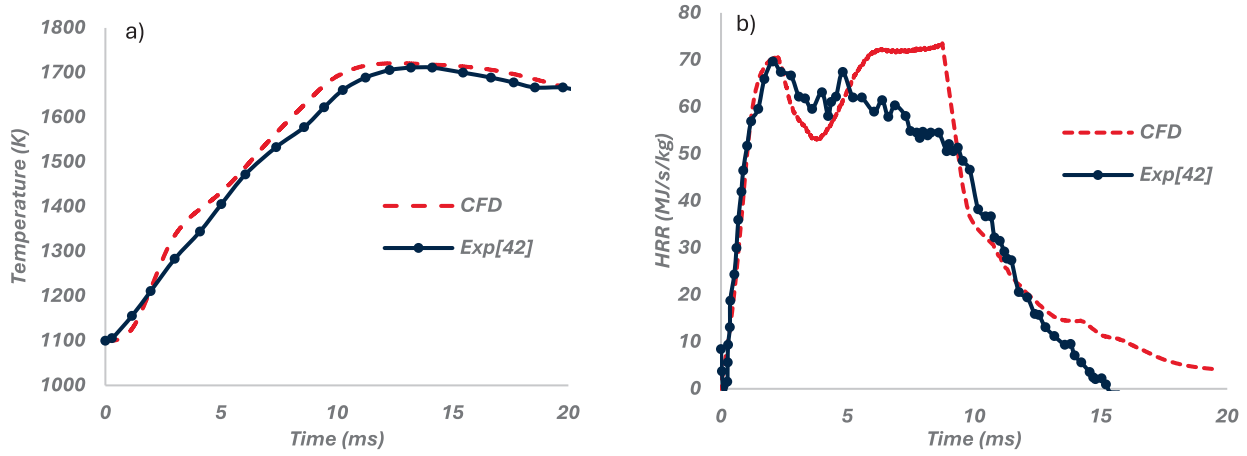

Fig. 7. Comparison of the H_2 jet ignition in Ar-O_2 medium of current CFD and experimental data adopted from Mansor et al. [40] (Ar mass rate = 90%; T_i = 1100 K; P_i = 4 Mpa; P_{inj} = 8 Mpa; and d_N = 0.8 mm): a) Temperature, b) HRR.

GT-Suite simulations are in good convergence.

Open-cycle simulation results, presented in Fig. 8, serve two purposes: (i) they validate the whole modelling framework by cross-verifying the outputs of the 3D CFD and 1D simulation domains; and (ii) they establish a reliable baseline for understanding the in-cylinder mixture formation processes discussed further.

Building on the validated combustion and valve flow models, full-cycle simulations are performed for the same reference point. Fig. 9a depicts the HRR, along with injection mass flow rates and TKE for SOI of −15° CA ATDC. There are three distinct peaks in the HRR profile. The first corresponds to the premixed combustion phase, and the second peak is associated with the impact of fuel jets on the piston's top surface. The third peak is attributed to the collision of fuel jets with the cylinder liner. Fig. 9b illustrates the corresponding H_2 mole fraction along the chamber's central plane which aligned with these HRR peaks, thus further validating them. Jet impact with solid walls lead to flame quenching and results in decreasing HRR. This phenomenon highlights that piston crown shape is an important design parameter for controlling HRR during fuel injection in jet ignition mode.

TKE and H_2 mass flow rate demonstrate strong correlation. TKE

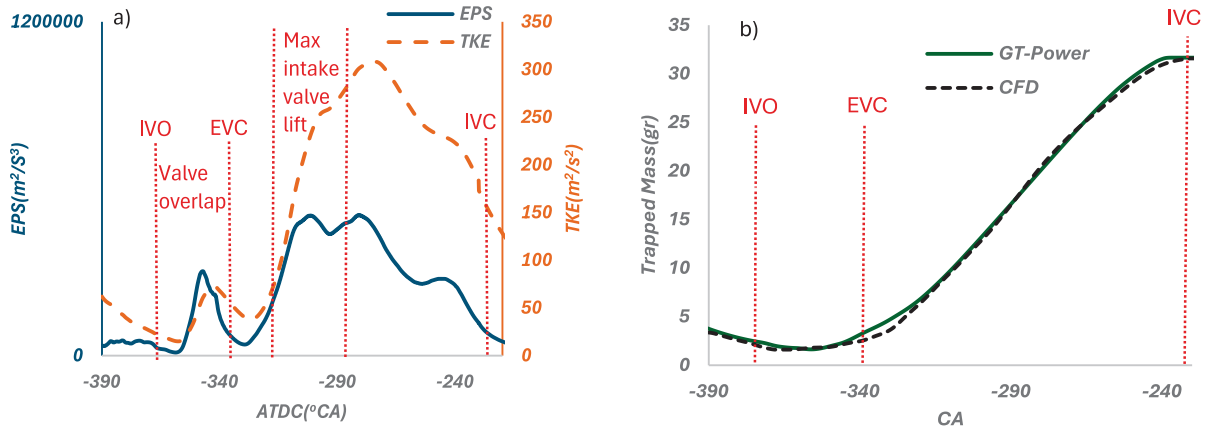

Fig. 8. In-cylinder TKE,ε and trapped mass and its comparison to 1D-GT Suite: a) In-cylinder ε and TKE, b) In-cylinder trapped mass.

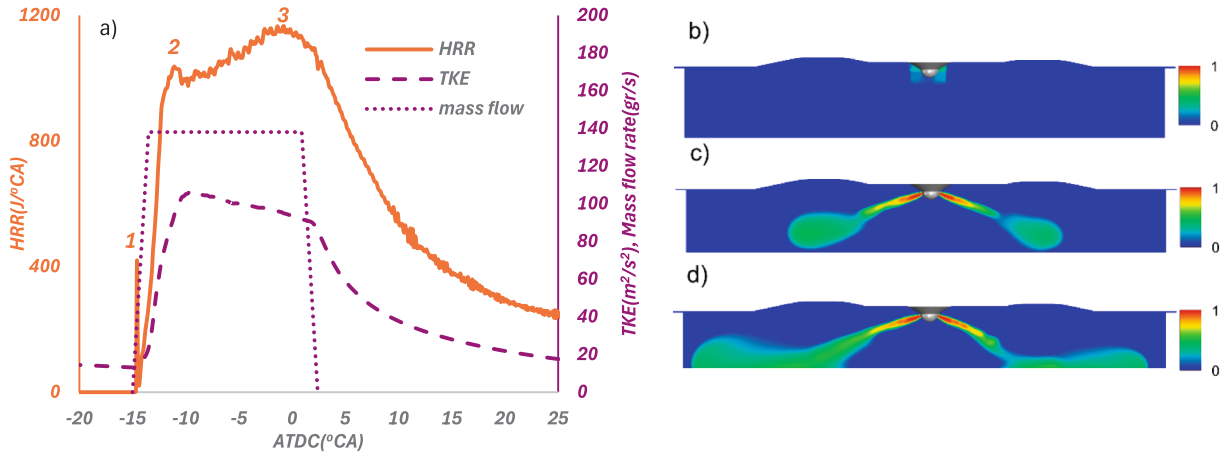

Fig. 9. HRR, TKE and injection mass flow rate for SOI = 15° CA BTDC; Cd = 0.8; Ar rate = 90%; λ = 1.1: a) HRR, TKE and H_2 mass flow rate, b) H_2 mole fraction at the first peak of HRR curve (14.88° CA BTDC), c) H_2 mole fraction at the second peak of HRR curve (11° CA BTDC), d) H_2 mole fraction at the third peak of HRR curve (0.6° CA BTDC).

mainly originates from the interaction between high-velocity fuel jets and the surrounding medium. However, there is a delay in peak of TKE compared to maximum mass flow rate. This is mainly because of the expansion of burned gases and the acceleration of unburned regions generate additional velocity fluctuations and further increase TKE.

3.4. Effects of SOI and nozzle discharge coefficient (C_d)

Fig. 10 illustrates the influence of SOI on the HRR and TKE for C_d of 0.8 and Ar rate of 90%. Both the first and second peaks in HRR increase with advancing injection timing. The ignition delay is longer for earlier SOIs, due to lower in-cylinder temperature before ignition. This extended delay allows a larger accumulation of premixed H_2 fraction,

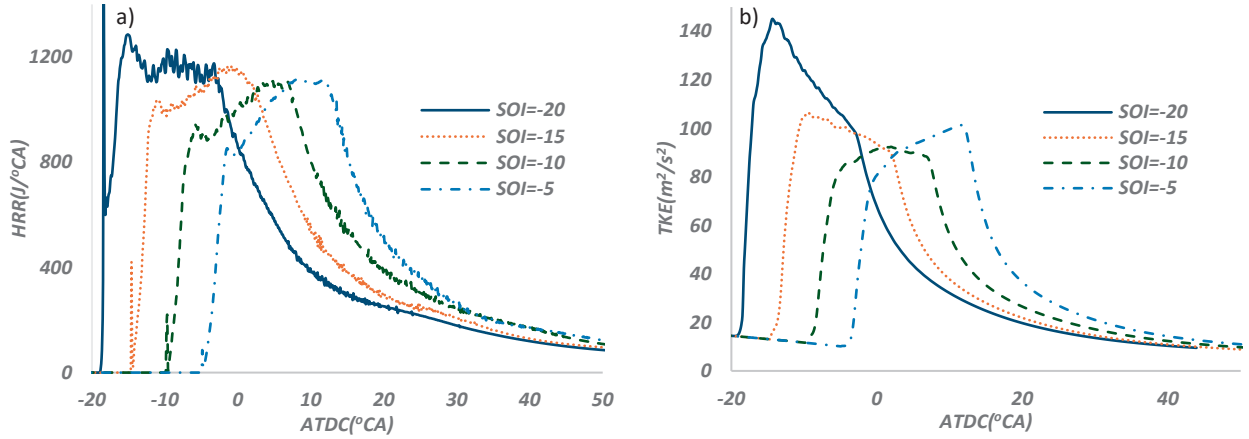

Fig. 10. The effect of SOI on HRR and TKE for Cd = 0.8; Ar rate 90%; and λ = 1.1: a) HRR, b) TKE.

resulting in a higher phase one peak HRR.

Under advanced SOIs, the jets have more time to penetrate and develop before the piston impact, resulting in an expanded flame front. Consequently, the jet flame area is increased, and higher HRR is observed for the second phase of combustion. Note that the magnitude of the third peak remains largely unaffected by SOI, because the diffusion flame area near the liner is almost constant.

The evolution of TKE in Fig. 10b highlights the distinct contributions of jet-induced turbulence and combustion-induced expansion, which vary significantly with SOI. For the earliest injection timing (SOI = −20° CA), the rapid increase in TKE occurs well before the main rise in HRR, indicating that the peak in TKE is largely established prior to significant heat release, confirming the dominance of jet-induced turbulence. For SOI = −15° CA, the onset of TKE growth still precedes the main HRR peak but shows increasing overlap with the combustion phase, suggesting a combined influence of jet-induced turbulence and early combustion-induced expansion.

In contrast, for later injection timings (SOI = −10° and −5° CA), the increase in TKE occurs concurrently with or after the onset of combustion, as indicated by the delayed rise relative to HRR. This shift in timing demonstrates that turbulence generation is increasingly governed by combustion-induced expansion rather than purely by jet momentum. In particular, for SOI = −5° CA, the negligible ignition delay leads to immediate coupling between heat release and flow acceleration, resulting in a TKE peak that is strongly influenced by volumetric expansion and occurs later in the cycle. These observations indicate that advancing SOI promotes turbulence dominated by jet–flow interactions, whereas retarded SOI shifts the primary turbulence generation mechanism toward combustion-driven expansion.

Fig. 11 reveals a strong correlation between ignition delay and mean in-cylinder temperature (two onsets shown @SOI and @SOC). Note, that minimum auto-ignition temperature of H_2 at corresponding mixture conditions is around 850 K[39]. However, the ignition delay at this temperature exceeds 10 ms, equivalent to over 60° CA at 1,000 rpm, resulting in predominantly uncontrolled premixed combustion rather than the desired jet ignition mode. Stable H_2 combustion within the jet ignition regime needs an average in-cylinder temperature at SOI of over 1150 K, enabling ignition delays below 0.5 ms (3° CA at 1,000 rpm). Importantly, Fig. 11 informs the ignition delay of 2.7° CA (0.45 ms) at SOI = −25°, which is approximately 12.5% larger than reported in jet-chamber experiments at similar mixture conditions by Mansor et al. [40]. The discrepancy between the present results and the referenced study [40] can be attributed to geometric and mixing-related scaling effects associated with the larger engine bore (200 mm vs. 80 mm). While the thermal boundary layer thickness scales with thermal

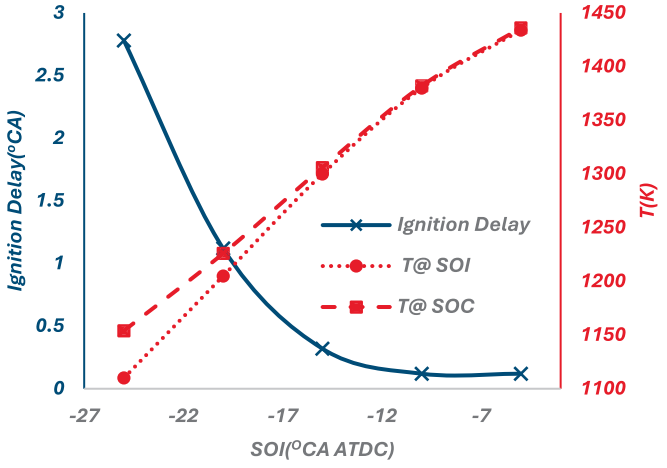

Fig. 11. Ignition delay and average in-cylinder temperature for different starts of injection at C_d = 0.8; Ar rate = 90%;.λ = 1.1

diffusivity and characteristic time ($\delta_t \sim \sqrt{\alpha t}$), the reference study employed a stirrer operating at 8000 rpm prior to injection, resulting in a characteristic mixing time scale significantly shorter than that of the present engine operating at 1000 rpm. This promotes a nearly uniform temperature field in the smaller chamber. In contrast, the larger bore and lower rotational speed in the present configuration lead to substantially longer mixing time scales, which are not commensurate with the available compression time. Consequently, incomplete thermal homogenization results in increased spatial temperature stratification. As a result, the H_2 jet may interact with locally cooler gas pockets, which leads to the observed increase in ignition delay.

The nozzle discharge coefficient (C_d) determines the instantaneous injection flow rate, governing jet penetration and subsequent combustion characteristics. Previous studies by Peters et al. [41] have reported a C_d value of 0.44 for direct H_2 injection into an argon–oxygen environment using a single-hole nozzle injector. However, the effective C_d is a design parameter of the injector and needs to be explored to determine the optimum injector tip to match the given combustor.

Fig. 12 illustrates the influence of C_d on HRR and combustion efficiency. A reduction in C_d decreases the effective flow area of the injector, which lowers both the mass flow rate and the jet exit velocity. As a result, the momentum flux of the jet is reduced, leading to weaker jet penetration and diminished entrainment of surrounding O_2 into the hydrogen plume.

While a longer injection duration compensates for the reduced mass flow rate to maintain the same total injected fuel, it does not recover the loss in jet momentum. Consequently, the mixing process becomes less efficient, particularly during the mixing-controlled combustion phase. This results in slower flame propagation and an extended combustion duration, as reflected by the broader and lower HRR profiles observed at lower C_d values. For example, duration extends from 18° CA at C_d = 0.8 to 36° CA at C_d = 0.4.

Fig. 12a shows that the SOC is not influenced by the H_2 flow rate (C_d). This observation suggests that auto-ignition is dominated by chemical kinetics, which are highly sensitive to temperature and pressure, rather than to the aerodynamic characteristics of the injected jet. The jet momentum and mixing processes strongly influence subsequent flame development and heat release, but the onset of combustion is controlled by the local thermochemical conditions established prior to ignition.

Fig. 12b shows combustion efficiency as a function of C_d and SOI. Combustion efficiency decreases with lower C_d values, with the peak observed near SOI = −20° CA ATDC across all cases. The maximum efficiency does not exceed 0.86, suggesting that H_2–O_2 mixing remains suboptimal. This is likely due to the adopted flat-piston geometry and will be discussed more thoroughly in the next section.

3.5. *Effects of unburned H_2 on next-cycle performance*

In a closed-loop APC, any unburned H_2 will be recirculated and burned during the premixed phase of the next cycle. To investigate this phenomenon, the influence of H_2 availability at the intake port is examined. Accordingly, the mass fractions of species are modified to 88.86% Ar; 0.07% H_2; 0.09% H_2O; and 10.98% O_2. This modification represents the assumption that 8% of the H_2 mass remains unburned in each cycle and re-enters the system through the intake port. All other boundary conditions are kept unchanged, as presented in Table 4.

Fig. 13 presents the in-cylinder pressure and PRR versus CA for different SOI timings under conditions where the aspirated charge contains residual unburned H_2 from previous cycles.

It is evident from Fig. 13 that an SOI of −20° CA results in excessive PRR, violating the assumed durability limit of 10 bar/°CA [42] over the major part of the heat release. A distinct initial PRR peak is observed across all SOI timings, consistently associated with premixed H_2 combustion. This peak remains below the critical threshold, indicating that

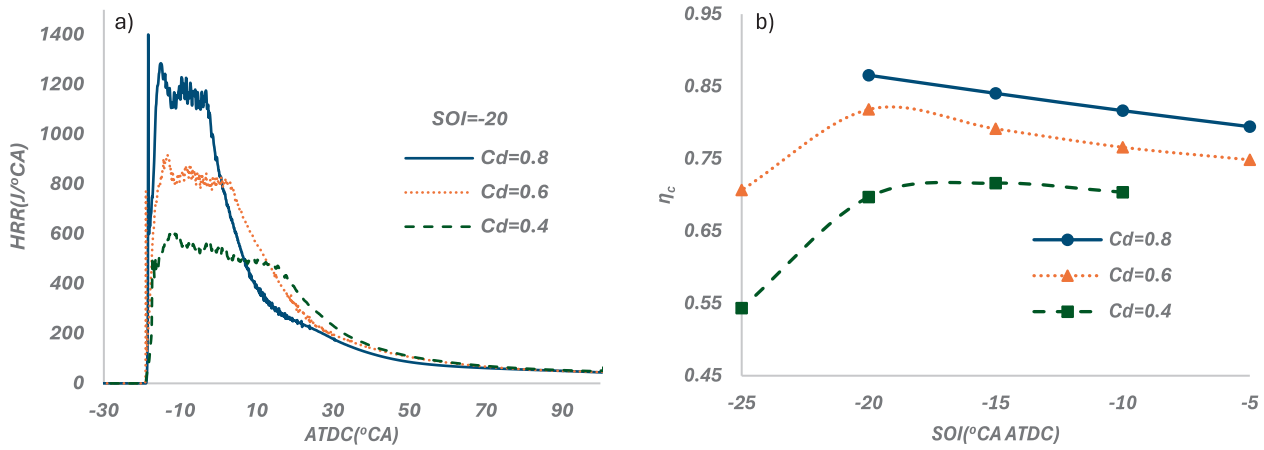

Fig. 12. The effect of C_d on HRR and combustion efficiency for Ar rate = 90%; λ = 1.1: a) HRR, b) combustion efficiency.

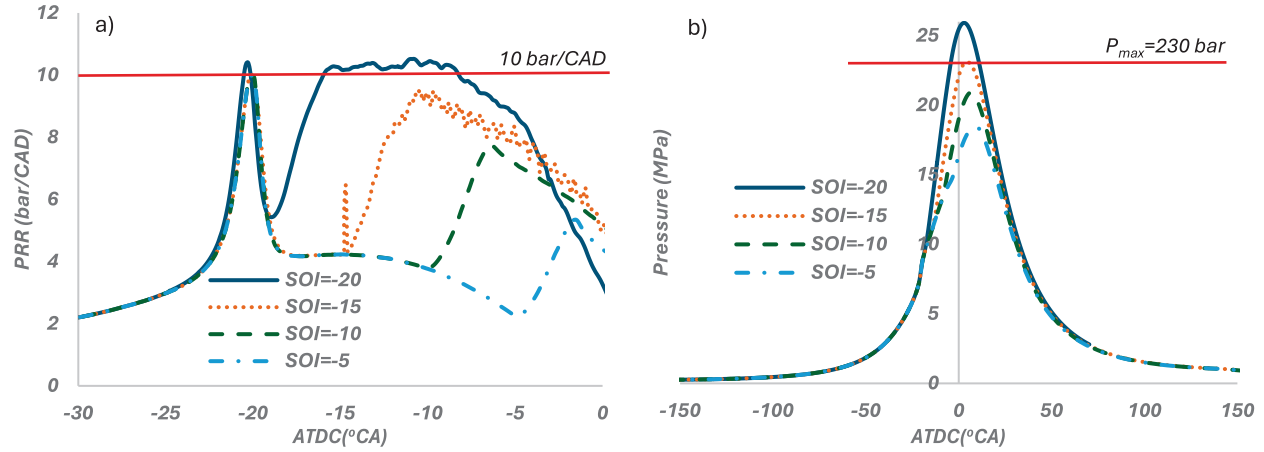

Fig. 13. The in-cylinder pressure and PRR for various SOI timings with 10% unburned H_2 at C_d = 0.8; Ar rate = 90%; λ = 1.1: a) PRR, b) In-cylinder pressure.

the carryover of 8% unburned H_2 (≈30 mg) represents acceptable combustion losses from the perspective of mechanical safety.

Importantly, the presence of a distinct premixed combustion phase reduces the ignition delay of the main combustion event. Unlike the H_2-free case, combustion begins almost immediately after fuel injection, regardless of injection timing. This behaviour is explained by the interaction between the H_2 jet and the hot combustion by-products generated during the premixed phase, which collectively promote rapid auto-ignition.

This effect is evident in the in-cylinder pressure traces, which show a characteristic step increase of 10–13 bar compared to the baseline case without residual H_2. The pressure jump becomes more pronounced at earlier injection timings, where advanced combustion phasing further steepens the pressure gradient. Notably, both the PRR and peak pressure limits are exceeded at SOI of −20° CA, indicating the need for retarding injection phasing, especially under conditions where incomplete

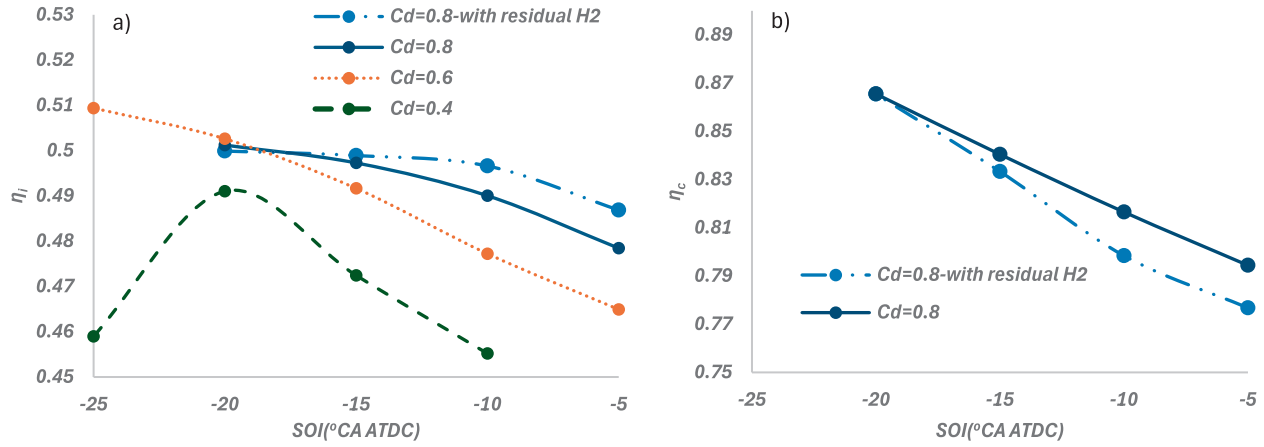

Fig. 14. The effect of unburned H_2 at intake on combustion efficiency and engine indicated efficiency for different C_d, Ar rate = 90%; λ = 1.1, a) Engine indicated efficiency, b) Combustion efficiency.

combustion may occur.

Retarded injections negatively affect engine indicated efficiency (η_i), due to less optimal combustion phasing. However, Fig. 14a shows that under conditions with residual H_2, this efficiency penalty is negligible (less than 0.2 percentage points) unless SOI is adjusted beyond the range of −20° to −10° CA. This observed insensitivity suggests that SOI control becomes less critical for overall APC efficiency calibration, as the inherent tendency of the combustion chamber towards incomplete combustion becomes the dominant limiting factor.

Regarding combustion efficiency (η_c), its decline with decreasing C_d is already observed in Fig. 12. Fig. 14b builds on this by incorporating the effect of residual H_2. It is evident that the presence of H_2 at the intake has no significant effect on η_c, despite substantially higher bulk gas temperatures during the main combustion phase, caused by the early burn of the premixed fraction. This finding indicates that efficient O_2 mixing within diffusion flames is more critical than either mean temperature or injection timing when seeking to improve combustion completeness.

Fig. 15 further supports this conclusion by providing a spatial analysis of fuel–oxidiser mixing quality and post-injection combustion activity. Specifically, the O_2 mole fraction is used as a representative indicator of local oxidiser availability, while the OH mole fraction serves as a proxy for active flame front regions. The results correspond to a representative operating point with best efficiency under permissible PRR and peak pressure limits, defined by $C_d = 0.6$ and SOI = −20° CA.

As shown, the flame front originates around the H_2 jet during injection (Fig. 15a) and expands rapidly due to the high jet momentum (Fig. 15b). Following the end of injection (Fig. 15c) and into the expansion stroke, the OH mole fraction decreases significantly, reflecting a decline in HRR as both the temperature drops and H_2–O_2 mixing weakens.

Notably, Fig. 15d shows a substantial accumulation of unreacted O_2 in the central region of the combustion chamber, where the H_2 momentum and diffusivity are insufficient to promote effective mixing and oxidation. This amount of unreacted O_2 at 35 CA ATDC equals 40% of total available oxygen at IVC which shows weak mixing of H_2 with O_2 after end of injection. This accounts for the late-stage decay of HRR, which both extends the combustion duration and reduces combustion efficiency.

This spatial decoupling of fuel and oxidiser reinforces the importance of local jet dynamics and stratification in determining combustion efficiency, and ultimately explains the results observed for different C_ds and SOIs (Fig. 14). In a nutshell, both advancing the injection timing and increasing the C_d improves the jet inducted turbulence (Fig. 10), which translates to higher mixing intensity. However, this improvement is not sufficient to achieve complete fuel oxidation, as PRR and peak pressure become the limiting factors. Ultimately, further improvements in combustion efficiency cannot be achieved through injection parameter calibration alone. Instead, priority should be given to the geometrical optimisation of jet–piston bowl interactions, which represents a tangible direction for future research.

3.6. *Remarks on the influence of argon ratio and mixture lambda*

Maximising the in-cylinder argon concentration is essential for APC thermodynamic efficiency. The study by Ahammed et al.[32] identified optimal efficiency conditions at a lambda value of 1.1 and an argon rate of 90%, which forms the baseline for the present study. However, those 1D thermodynamic simulations focused solely on cycle efficiency with non-predicative HRR from a diesel engine, while assuming a negligible impact on combustion behaviour, particularly with regard to H_2 diffusion jet phenomenology. The previous sections already verified that this assumption is an oversimplification and inauthentic. A lambda sweep and an argon rate sweep enable further insights into the influence of mixture composition on combustion performance. Both sweeps are achieved by varying the APC system pressure while adjusting the oxygen mass to match the nominal conditions in all the other parameters. Table 6 lists the governing input parameters changed for the open-cycle CFD simulation: all other values, including H_2 injection parameters, are kept constant as provided in Table 4.

Fig. 16 juxtaposes the engine efficiency indicators with HRR for different λ values. Note that thermodynamic efficiency shows negligible variation as the argon dilution remains unaffected. The small increase in thermodynamic efficiency from lambda 1.1 to 1.4 is the result of changes in combustion phasing.

The longer ignition delay with increasing lambda, evident in

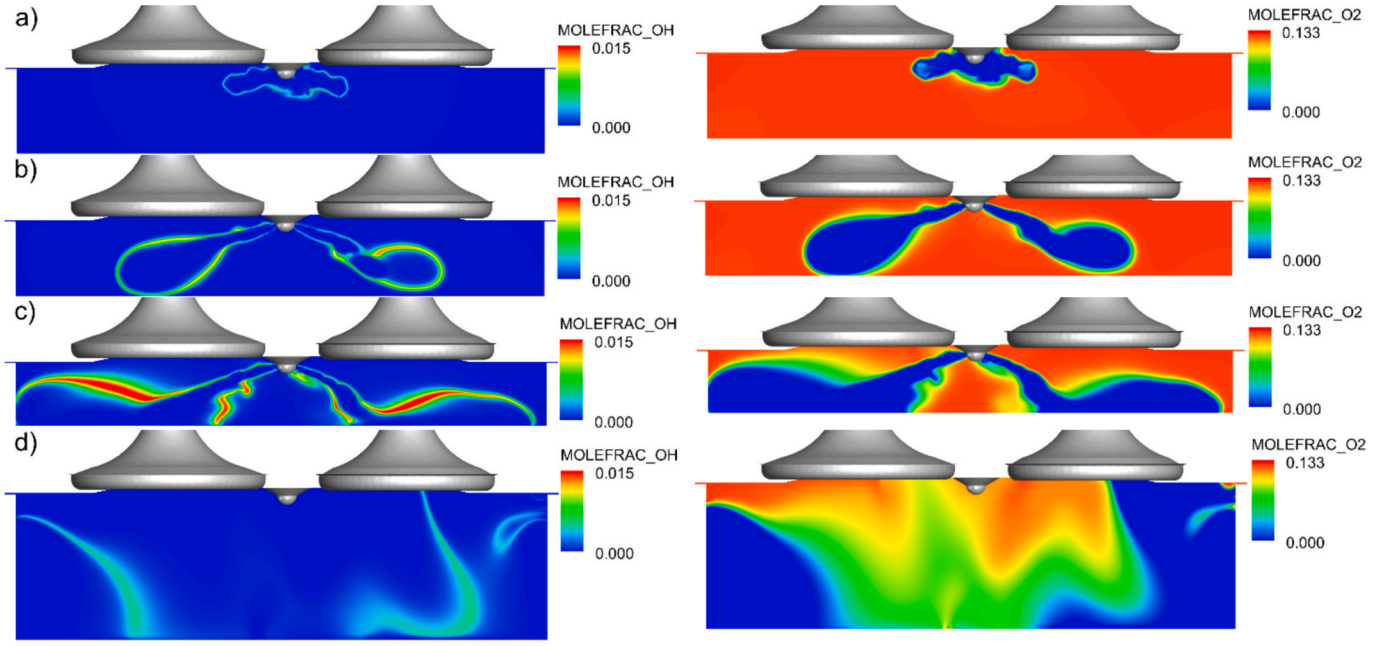

Fig. 15. The OH (left) and O_2 (right) mole fraction in the mid-plane of the combustion chamber for the best efficiency operating point (SOI = -20 and $C_d = 0.6$); Ar rate = 90%; λ = 1.1: a) CA = -18.5° ATDC (the first peak of HRR), b) CA = -13.5° ATDC (the second peak of HRR), c) CA = 5° ATDC (the end of injection), d) CA = 35° ATDC.

Table 6
Relevant quantities changed in the lambda and Ar rate sweeps: bolded values represent nominal conditions; all remaining values are according to Table 4.

	Lambda sweeps					Ar sweeps	
Case number	**1**	2	3	4	5	6	7
Lambda	**1.1**	1.3	1.4	1.5	1.6	**1.1**	
Ar rate (%)	**90**					85	95
Intake P(bar)	**3,75**	4.37	4.72	5.06	5.4	2.8	7.625
Exhaust P(bar)	**4.03**	4.65	5.01	5.36	5.72	3.09	8.025
O_2 trapped mass(mg)	**3360**						

Fig. 16b, reflects both chemical and physical contributions. From a chemical perspective, reduced temperature (due to decreased specific heat ratio for higher λ) slows down reaction kinetics, thereby extending the ignition delay. However, the increase in ignition delay alone does not explain the non-linear trend in combustion efficiency shown in Fig. 16a.

A key additional factor is the evolution of physical mixing processes under varying λ. As λ increases, the corresponding rise in in-cylinder pressure (Table 6) suppresses jet penetration and radial dispersion. This leads to reduced entrainment of O_2 into the hydrogen jet and delays the formation of locally flammable mixtures. Therefore, part of the observed ignition delay must be attributed to mixing-limited ignition, rather than purely chemical kinetics.

Increased ignition delay and the corresponding rise in premixed heat release increases the share of premixed fraction and disrupts the following mixing-controlled combustion phase due to intensifying HRR fluctuations. The latter is attributed to the already-mentioned, combustion invoked turbulence, as discussed in relation to Fig. 10.

Fig. 17 illustrates how H_2 jet development is impacted by increased compression pressure arising from the λ sweep. Shown is the equivalence ratio isosurface of 0.4, captured at a fixed reference point (2.5° CA after SOI) across different λ cases. The comparison reveals a clear trend: as injection backpressure increases, jet penetration is progressively diminished and fuel–air mixing becomes less effective, affecting ignition delay. The radial dispersion of the fuel plume is visibly suppressed, which together with the increased share of premixed HRR creates complex patterns of HRR for mixing-controlled combustion, responsible for non-linearities in combustion efficiency. These results highlight a critical influence of in-cylinder pressure on jet development—a factor that has received limited attention in existing literature, and particularly none in the context of H_2 direct injection under argon-diluted conditions.

Fig. 18 depicts the results of the argon dilution rate sweep, and also shows engine and combustion efficiencies for different Ar mass ratios at the same H_2 injection. Although combustion efficiency decreases with increasing Ar mass rate (due to the lower oxygen mass fraction and higher in-cylinder pressure), engine efficiency increases at higher Ar mass rates because argon has a higher specific heat ratio than oxygen. Engine efficiency reaches 56% at 95% Ar mass rate, which is the highest among the cases studied. However, the corresponding low combustion efficiency of 57% makes this condition impractical for real-world applications. Therefore, operating with a leaner mixture at higher Ar mass rates may provide a viable solution to achieve high efficiency for both engine and combustion.

Fig. 19 summarises the effects of total fuel ratio($\frac{m_{H_2}}{totalincylindertrapedmass}$), supporting the interpretation of λ and Ar rate effects. Total fuel ratio is defined to decouple the influence of oxygen dilution (λ) from that of the argon dilution rate, enabling a clearer phenomenological interpretation. While the λ is maintained at 1.1 during the Ar sweep, an Ar rate of 90% is used for the λ sweep. The pivotal point of two variational curves corresponds to Ar rate of 90% and$\lambda = 1.1$ in all parts of this figure.

Fig. 19a shows in-cylinder pressure at the start of injection. According to Table 6, higher in-cylinder pressure is needed for a higher Ar rate and higher λ in order to keep O_2 trapped mass constant in all conditions. So, the in-cylinder pressure shows the increasing trend for both Ar rate and λ increase.

Although, in-cylinder temperature increases at higher Ar rates due to

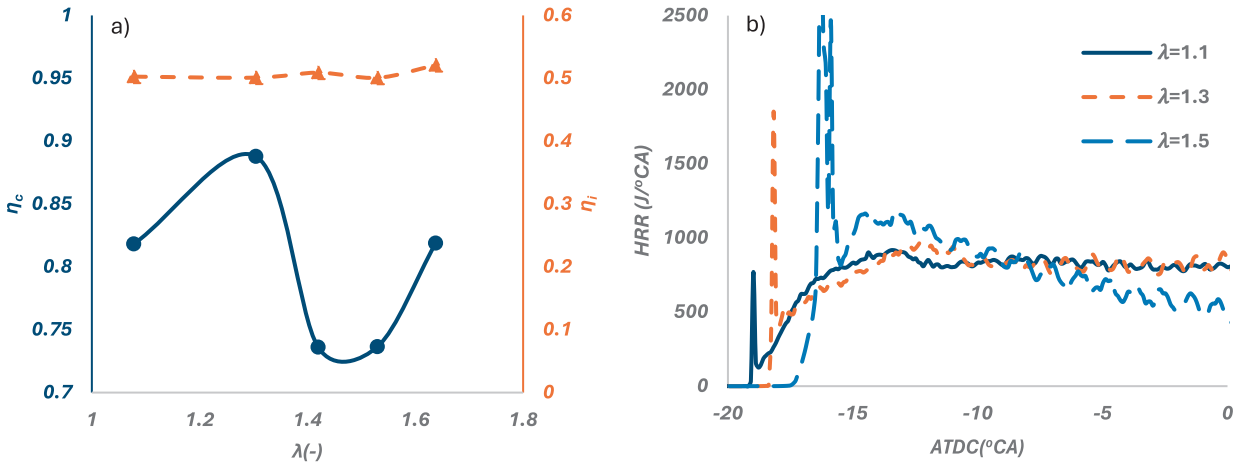

Fig. 16. The effect of λ on combustion and engine indicated efficiency with the same H_2 injection for $C_d = 0.6$; Ar rate = 90%; SOI = -20° CA ATDC (HRR of 1.4 and 1.6 excluded for better visibility): a) combustion efficiency and engine indicated efficiency, b) HRR.

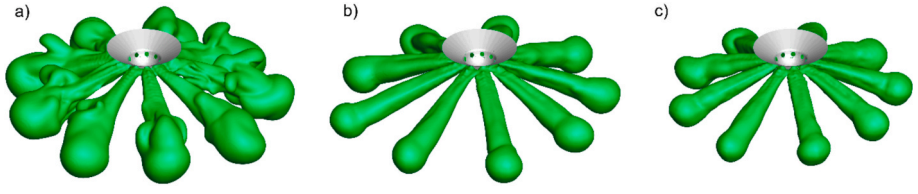

Fig. 17. Isosurfaces of equivalence ratio of 0.4 at different λ for CA = -17.5° ATDC; SOI = -20°; Cd = 0.6; and Ar rate = 90%: a) λ = 1.1, Pintake = 3.75 bar, b) λ = 1.4, Pintake = 4.37 bar, c) λ = 1.6, Pintake = 5.06 bar.

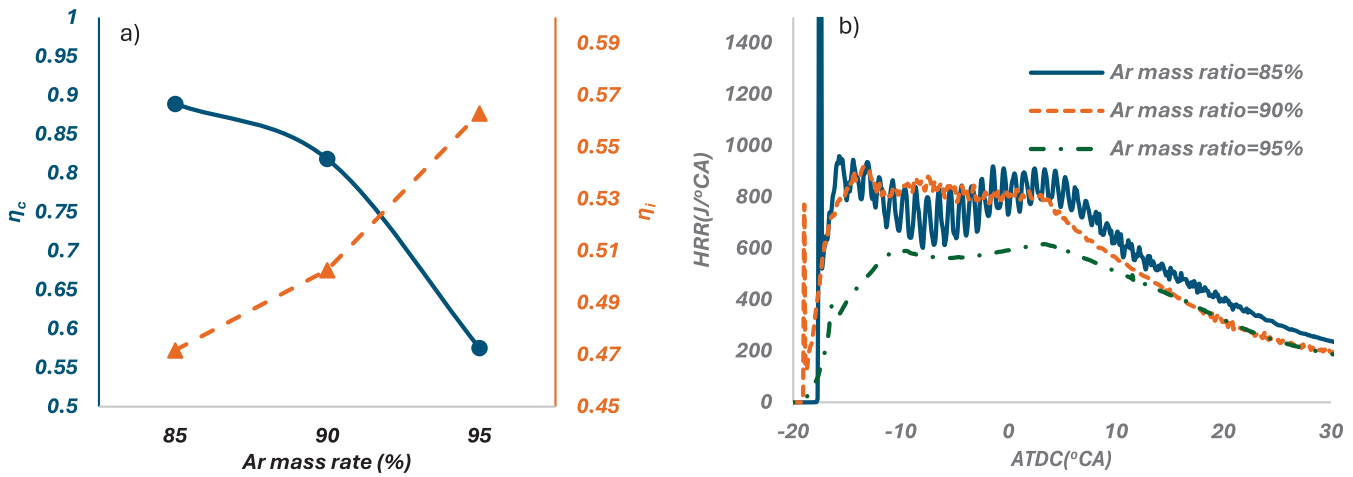

Fig. 18. The effects of Ar mass rate on combustion and engine indicated efficiency with the same cycle pressure for Cd = 0.6; λ = 1.1; SOI = -20° CA ATDC: a) combustion efficiency and engine indicated efficiency, b) HRR.

higher specific heat of Ar, an opposite decreasing trend is observed at higher λ values as a result of the reduced specific heat ratio(Fig. 19b).

The elevated in-cylinder temperature tends to shorten the ignition delay, but higher in-cylinder pressure and increased Ar mass rate act in the opposite direction. On the other hand, at high Ar mass fractions, relative oxygen availability is reduced, and higher in-cylinder pressure confines jet development, as discussed in Fig. 17, thereby delaying the start of combustion. Due to these competing effects, the 90% Ar case exhibits the shortest ignition delay (1° CA), followed by the 95% Ar case (1.5° CA), indicating that the influence of in-cylinder temperature is greater than that of in-cylinder pressure (Fig. 19c). In contrast, the longer ignition delay observed for the 85% Ar case (2.4° CA) leads to a pronounced premixed combustion peak, followed by a fluctuating HRR during the mixing controlled phase (Fig. 18b).

On the other hand, there are no competing effects of in-cylinder temperature and pressure on SOC during the λ variation, and both parameters act in the same direction to retard SOC as λ increases. As shown in Fig. 19a and b, the in-cylinder pressure increases while the temperature decreases with increasing λ. Therefore, SOC is expected to be delayed at higher λ values, as illustrated in Fig. 19c.

The CA50 for the Ar rate in Fig. 19d follows the same trend as SOC, indicating that faster combustion requires a shorter ignition delay. However, due to the fluctuating HRR associated with the longer ignition delays at higher λ values, no clear trend in CA50 with respect to λ variation is observed. This suggests that the predictability of combustion phasing deteriorates when the ignition delay exceeds 1.5° CA, potentially leading to high cyclic variations.

Fig. 19e shows a similar decreasing trend in TKE at CA50 for both higher Ar rate and λ dilution, which is attributed to the higher in-cylinder pressure. Jet-induced turbulence decreases at higher in-cylinder pressures (Fig. 17), and this lower TKE reduces O_2 entrainment to the jet ignition, thereby lowering combustion efficiency (Fig. 18a). Consequently, the reduced combustion efficiency leads to lower in-cylinder temperatures at CA50, as shown in Fig. 19f.

4. Outlook and discussion

The key findings can be discussed in relation to both fundamental relevance and applied significance, this studýs two interconnected research objectives. The study also identifies relevant limitations that determine the outlook for further research.

4.1. Fundamental relevance

The phenomenology of H_2 jet combustion in a closed-loop Argon combustor considers three distinctive phases, which further drive relevant fundamental insights regarding ignition delay and combustion efficiency.

The first phase corresponds to the rapid combustion of premixed H_2, either formed during the ignition delay or carried over as residuals from the previous cycles.

The second mixing-controlled phase originates from the oxidiser entrainment into the developing jet. The heat release is intensified by jet-driven turbulence and boundary layer interaction with the moving piston crown.

The third phase is the combustion decay, governed by the loss of jet momentum following the end of injection. Jet–liner interactions further suppress residual mixing, limiting final-stage oxidation.

The study reveals that a modest increase of 20 bar in backpressure can delay ignition by up to 2° CA, due to reduced radial jet dispersion. Under argon-induced high-temperature compression, chemical ignition delay becomes negligible once in-cylinder temperatures exceed 1300 K, corresponding to SOIs later than 15° CA (BTDC) at the reference mixture composition.

High-pressure direct injection of H_2 in an argon-diluted oxygen mixture suffers from substantial combustion losses, linked to local oxygen deficit in the final combustion phase. As with ignition delay, flame quenching is not thermally limited but results from weak dispersion of jets, accumulating H_2 at the liner, leaving unreacted oxygen near the chamber centre. This distribution is, however, specific to the adopted flat piston configuration.

4.2. Applied significance

Building upon the above phenomenological insights, the study enables formulation of practical calibration strategies for future argon power systems considering direct H_2 injection.

Although the closed-loop architecture recovers unburned H_2 via charge recirculation, maintaining high combustion efficiency remains critical to avoid breaching constraints on peak pressure/temperature and PRR. The presence of 8% unburned H_2 at the intake has a negligible impact on indicated efficiency (<0.2 percentage point). However, it significantly increases premixed heat release, causing PRR to reach the 10 bar/°CA limit. This defines a practical lower boundary for combustion efficiency at ~92%, below which stability and safety constraints are compromised.

Increasing the injector nozzle discharge coefficient or advancing SOI enhances mixing and combustion efficiency but results in excessive PRR during the main heat release phase. At the reference airpath setting (λ = 1.1, 90% Ar), meeting the 230 bar peak pressure boundary requires

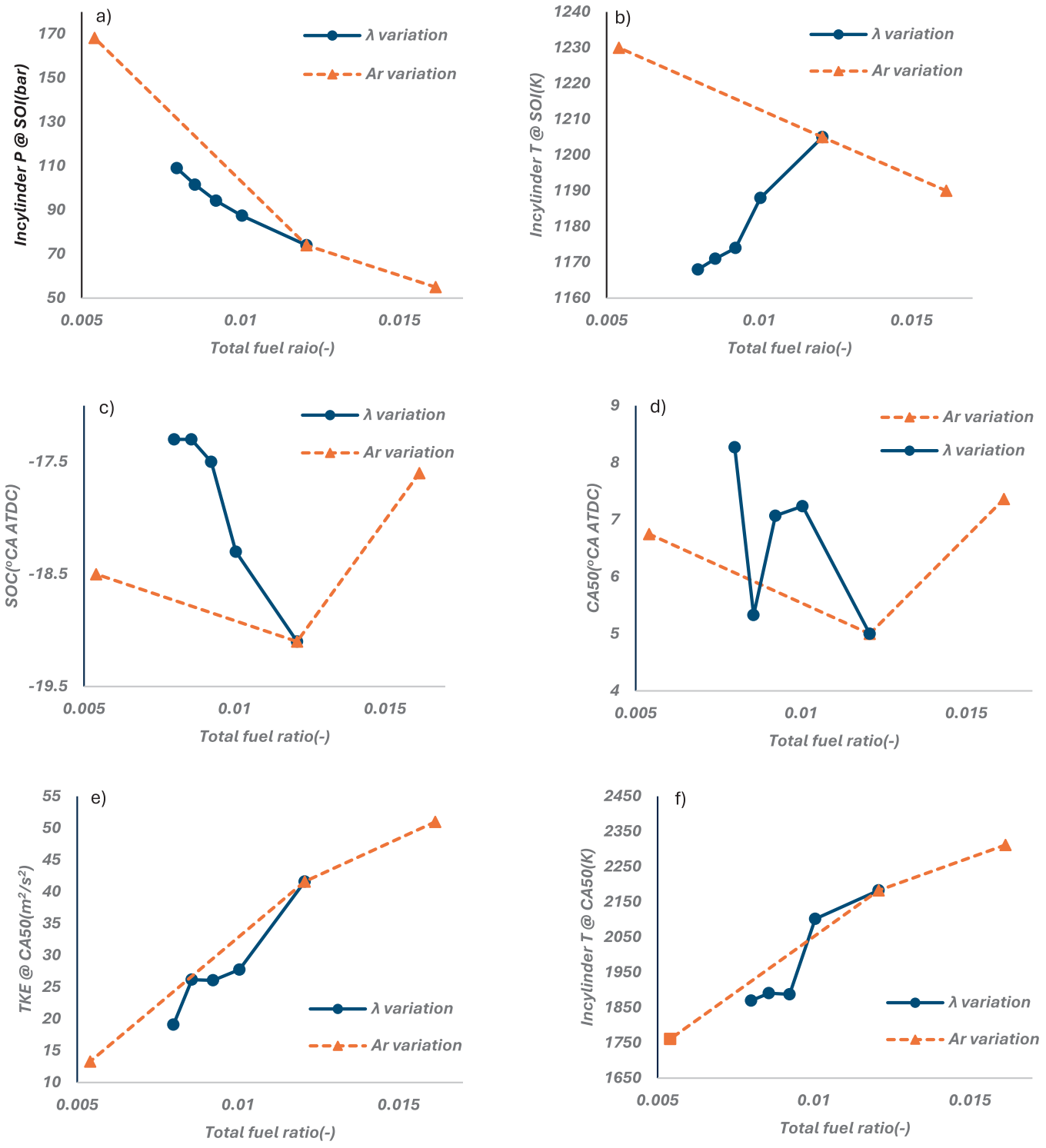

Fig. 19. The variation of influential parameters with total fuel ratio for $C_d = 0.6$; SOI = -20° CA ATDC; and 382 mg H_2 injection: a) In-cylinder pressure @ SOI, b) In-cylinder temperature @ SOI, c) SOC, d) CA50, e) TKE @ CA50, f) In-cylinder T @ CA50.

limiting the discharge coefficient to 0.6, while maintaining the phasing-optimal SOI at −20° CA ATDC.

The combustion efficiency peaks at slightly leaner mixture (λ = 1.3), without disturbing the phasing calibration. However, the maximum value still falls 3.5 percentage points short of the 92% efficiency target. Thermodynamic efficiency at 90% argon rate reaches 51%, far from the envisioned 60%. Increasing the argon dilution to 95% relaxes the PRR and peak temperature constraints and elevates indicated efficiency to 56%. However, combustion efficiency suffers from increased injection backpressure, further limiting jet momentum and mixing quality.

4.3. Study limitations and outlook for further research

The relatively low efficiency observed in this study is attributed primarily to the use of flat piston geometry. This design choice was intentional, serving the core objective of establishing a reliable baseline for understanding in-cylinder mixing and combustion processes in APC engines, without the confounding influence of bowl-specific turbulence

structures.

While appropriate for isolating fundamental jet behaviour, the flat piston configuration is not optimal for combustion efficiency, especially in the context of mixing-limited post-injection oxidation, as demonstrated in the current results. This insight provides a solid foundation for the next phase of the iHAPC project [43], which consequently focuses on multi-dimensional optimisation of injector nozzle design and piston-bowl geometry. The current simulation framework enables this by extension to include rapid re-meshing and surrogate optimisation workflows [44], accelerating the exploration of complex design spaces.

5. Conclusions

Three distinct H_2 combustion phases are identified in the argon power cycle: (1) rapid premixed burn of H_2 residuals; (2) mixing-controlled heat release driven by jet–piston interaction; and (3) post-injection combustion decay limited by liner-induced momentum loss.

Ignition delay is governed by O_2 entrainment, along with chemical kinetics. Chemical delay becomes negligible at in-cylinder temperatures above 1300 K, while a 20-bar increase in injection backpressure can extend ignition delay by $\sim 2^\circ$ CA.

Flame quenching is non-thermal yet mixing-limited, with unburned H_2 accumulating at the liner and unreacted O_2 remaining near the chamber centre.

Combustion phasing is decoupled from airpath conditions, and instead controlled by injection timing and duration, enabling separate optimisation of phasing and thermodynamic efficiency.

Maintaining combustion efficiency above 92% is essential to prevent PRR from exceeding the 10 bar/°CA limit, even though recirculated unburned H_2 has minimal impact (<0.2%) on indicated efficiency.

Injector discharge coefficient must be limited to 0.6 to meet peak pressure limits (230 bar) at $\lambda = 1.1$ and 90% argon, while maintaining SOI at -20° CA for optimal phasing.

Increasing argon dilution to 95% raises thermodynamic efficiency to 56%, but significantly depresses combustion efficiency due to higher injection backpressure. The best observed trade-off at 90% argon and $\lambda = 1.3$ yields 51% thermodynamic efficiency.

Further efficiency gains require piston geometry optimisation, because a flat piston limits mixing during late combustion. Upcoming work will integrate rapid geometrical optimisation and improved injector/jet modelling to establish optimal hardware design.

CRediT authorship contribution statement

Iman Chitsaz: Writing – review & editing, Writing – original draft, Visualization, Validation, Software, Methodology, Investigation, Formal analysis, Data curation, Conceptualization. **Alireza Kakoee:** Software. **Sajid Ahammed:** Software. **Mahdi Salahi:** Validation. **Amin Mahmoudzadeh Andwari:** . **Zeeshan Ahmad:** Writing – review & editing. **Jari Hyvönen:** Writing – review & editing, Supervision, Resources, Project administration, Methodology, Investigation, Funding acquisition, Conceptualization. **Maciej Mikulski:** Writing – review & editing, Supervision, Resources, Project administration, Methodology, Investigation, Funding acquisition, Conceptualization.

Declaration of competing interest

The authors declare the following financial interests/personal relationships which may be considered as potential competing interests: Iman chitsaz reports financial support was provided by Business Finland. Business Finland has supported iHAPC project which current paper is one of the outcome of this research. If there are other authors, they declare that they have no known competing financial interests or personal relationships that could have appeared to influence the work reported in this paper.

Acknowledgments

This research was conducted as a part the Integrated Hydrogen–Argon Power Cycle (iHAPC) project, co-funded by Business Finland (ref. 10309/31/2023).

The authors also acknowledge CSC for providing high-performance computational infrastructure.

Data availability

The data that has been used is confidential.

References

[1] Liu L, Shao W, Yan Y, Liu D, Zhang J. Intelligent self-adaption of marine engine degradation based on a digital-twin model. Energy Convers Manag Oct. 2025;341. https://doi.org/10.1016/j.enconman.2025.119995.
[2] Madadi MH, Chitsaz I. Improving fuel efficiency and durability in fuel cell vehicles through component sizing and power distribution management. Int J Hydrogen Energy Jun. 2024;71:661–73. https://doi.org/10.1016/J.IJHYDENE.2024.05.276.
[3] Wang C, Deng J, Dibble RW, Li L. A novel hydrogen energy storage system: Power regeneration employing a 70 % NITE Argon Power Cycle hydrogen-fueled engine. Int J Hydrogen Energy Oct. 2025;178. https://doi.org/10.1016/j.ijhydene.2025.151531.
[4] Sajid Ahammed, "Hydrogen-Argon Power Cycle (HAPC) on a Wartsila medium-speed engine: an Investigation using 1D-Simulation," Master's thesis in Energy Technology, University of Vaasa, Vaasa, 2025.
[5] Liu L, Xu Z, Wang L, Wang Y, Li H, Wu Y. Theoretical analysis on high-efficiency combustion and emissions reduction strategy of ammonia-diesel direct injection marine medium-speed engines under energizing-intensifying composite combustion mode. Appl Therm Eng Nov. 2025;278. https://doi.org/10.1016/j.applthermaleng.2025.127391.
[6] J. Kim, R. Scarcelli, G. Beardsell, T. Strickland, C. Nilsen, and M. Sierra Aznar, "Modeling Pre-Chamber Assisted Efficient Combustion in an Argon Power Cycle Engine," in *SAE Technical Papers*, SAE International, Apr. 2024. doi: 10.4271/2024-01-2690.
[7] M. S. Aznar, "Numerical and experimental investigation of the Argon Power Cycle for power generation efficiency improvement and emissions reduction," University of California at Berkeley, Berkeley, 2018.
[8] M. Sierra Aznar, F. Chorou, F. Chorou, J.-Y. Chen, A. Dreizler, and R. W. Dibble, "Experimental and Numerical Investigation of the Argon Power Cycle," in *Internal Combustion Engine Division Fall Technical Conference*, American Society of Mechanical Engineers , Nov. 2018.
[9] A. Elkhazraji, "On Maximizing Argon Engines' Performance via Subzero Intake Temperatures in HCCI Mode at High Compression Ratios," King Abdullah University of Science and Technology, 2020. doi: https://doi.org/10.25781/KAUST-P7W86.
[10] A. M. Mohammed, J. B. Masurier, A. Elkhazraji, R. Dibble, and B. Johansson, "A path towards high efficiency using argon in an HCCI engine," in *SAE Technical Papers*, SAE International, Apr. 2019. doi: 10.4271/2019-01-0951.
[11] Shi S, Tomomatsu Y, Chaturvedi B, Aznar MS, Chen JY. Engine efficiency enhancement and operation range extension by argon power cycle using natural gas. Appl Energy Jan. 2021;281. https://doi.org/10.1016/j.apenergy.2020.116109.
[12] de Boer PCT, Hulet JF. Performance of a hydrogen-oxygen-noble gas engine. Int J Hydrogen Energy Jan. 1980;5(4):439–52. https://doi.org/10.1016/0360-3199(80)90024-5.
[13] Ikegami M, Miwa K, Shioji M. A study of hydrogen fuelled compression ignition engines. Int J Hydrogen Energy Jan. 1982;7(4):341–53. https://doi.org/10.1016/0360-3199(82)90127-6.
[14] Rentaro Kuroki, Akira Kato, Eiichi Kamiyama, and Daisaku Sawada, "Study of High Efficiency Zero-Emission Argon Circulated Hydrogen Engine," *SAE Technical Paper*, 2010.
[15] Killingsworth NJ, Rapp VH, Flowers DL, Aceves SM, Chen JY, Dibble R. Increased efficiency in SI engine with air replaced by oxygen in argon mixture. Proc Combust Inst Jan. 2011;33(2):3141–9. https://doi.org/10.1016/J.PROCI.2010.07.035.
[16] Erbao Zhang *et al.*, "Cyclic Variations of Argon Power Cycle Engine with Fuel of Hydrogen," in *International Powertrains, Fuels & Lubricants Meeting*, 2017, https://doi.org/10.4271/2017-01-2409. SAE Technical Paper 2017-01-2409, Ed., 2017.
[17] Li L, Gong Y, Deng J, Gong X. CO 2 reduction request and future high-efficiency zero-emission argon power cycle engine. Autom Innov Jan. 2018;1(1):43–53. https://doi.org/10.1007/s42154-018-0007-y.
[18] Jin S, et al. Knock control in hydrogen-fueled argon power cycle engine with higher compression ratio by water port injection. Appl Energy Nov. 2023;349. https://doi.org/10.1016/j.apenergy.2023.121664.
[19] W. Ding *et al.*, "Operating and Thermal Efficiency Boundary Expansion of Argon Power Cycle Hydrogen Engine," *Processes*, vol. 11, no. 6, Jun. 2023, doi: 10.3390/pr11061850.
[20] C. Wang, S. Jin, J. Deng, W. Ding, Y. Tang, and L. Li, "Future High-Efficiency and Zero-Emission Argon Power Cycle Engines: A Review," *International Journal of Automotive Manufacturing and Materials*, vol. 2, no. 2, Jun. 2023, doi: https://doi.org/10.53941/ijamm.2023.100002.

[21] Cui W, Wang C, Deng J, Su X, Wu Z, Li L. Effects of hydrogen and methane anti-knocking characteristics on the efficiency and power output in argon power cycle engines. Int J Hydrogen Energy Sep. 2024;83:70–8. https://doi.org/10.1016/j.ijhydene.2024.08.082.
[22] Ding W, Deng R, Deng J, Wang C, Li L. Combustion characteristics optimization and thermal efficiency enhancement by stratified charge of hydrogen direct injection for argon power cycle hydrogen engine. Int J Engine Res Aug. 2024;25(8):1461–75. https://doi.org/10.1177/14680874241233218.
[23] L. Kniestedt, W. Roßlau, K. Stenzel, M. Cech, M. Florian, and C. Reiser, "Argon Power Cycle (APC)-The way to zero emission ICEs," in *CIMAC CONGRESS*, BUSAN, Jul. 2023. [Online]. Available: https://www.cimac.com.
[24] Manuel Cech, Matthias Knape, Tom Wilfert, and Christian Reiser, "The Emission-free Hydrogen Closed cycle Engine," *MTZ worldwide*, Apr. 2021.
[25] N. M. Taib, M. R. A. Mansor, and W. M. F. W. Mahmood, "Combustion characteristics of direct injection hydrogen in noble gases atmosphere," in *IOP Conference Series: Earth and Environmental Science*, Institute of Physics Publishing, Apr. 2020. doi: 10.1088/1755-1315/463/1/012058.
[26] Taib NM, Mahmood WMFW, Mansor MRA. Combustion characteristics of hydrogen direct injection in a helium–oxygen compression ignition engine. Energy Rep Nov. 2022;8:494–511. https://doi.org/10.1016/j.egyr.2022.07.026.
[27] N. Mat Taib, W. M. F. Wan Mahmood, W. A. W. Ghopa, H. Köten, and M. R. Abu Mansor, "Numerical study of heat transfer of hydrogen combustion in noble gases atmosphere in compression ignition engine," *Int. J. Hydrogen Energy*, vol. 48, no. 74, pp. 28970–28979, Aug. 2023, doi: 10.1016/j.ijhydene.2023.04.071.
[28] H. S. Van Den Brink, "Exploring injection strategies for the Argon Power Cycle in CONVERGE CFD," Eindhoven University of Technology, 2022. [Online]. Available: www.tue.nl.
[29] Mikko Merikoski, "Parker Collaborates on Hydrogen-Argon Power Cycle Initiative for Sustainable Energy," https://www.parker.com/dk/en/about-parker/newsroom/news-release-details/hydrogen-argon-power.html.
[30] Katri Pehkonen, "Wärtsilä joins new consortium to explore hydrogen-argon power cycle for net-zero power generation," https://www.wartsila.com/media/news/26-11-2024-wartsila-joins-new-consortium-to-explore-hydrogen-argon-power-cycle-for-net-zero-power-generation-3586733.
[31] A. Kakoee *et al.*, "The interplay between combustion and component thermal loading in next generation marine engines employing reactivity-controlled compression ignition." [Online]. Available: https://ssrn.com/abstract=5297450.
[32] S. Ahammed, Z. Ahmad, A. M. Andwari, A. Kakoee, J. Hyvonen, and M. Mikulski, "Enabling near-zero emissions and superior efficiency in large-bore, medium-speed engines with a hydrogen-argon power cycle," in *17th International Conference on Engines and Vehicles*, Capri : SAE, Sep. 2025.
[33] Dong S, et al. A new detailed kinetic model for surrogate fuels: C3MechV3.3. Appl Energy Combust Sci Mar. 2022;9. https://doi.org/10.1016/j.jaecs.2021.100043.
[34] A. Kakoee *et al.*, "Start of Injection Influence on In-Cylinder Fuel Distribution, Engine Performance and Emission Characteristic in a RCCI Marine Engine," *Energies* , vol. 17, no. 10, May 2024, doi: 10.3390/en17102370.
[35] Stephen R. Turns, *An Introduction to Combustion: Concepts and Applications*, 2nd, illustrated ed. McGraw-Hill, , 2000.
[36] Chitsaz I, Saidi MH, Mozafari AA, Hajialimohammadi A. Experimental and numerical investigation on the jet characteristics of spark ignition direct injection gaseous injector. Appl Energy 2013;105:8–16. https://doi.org/10.1016/j.apenergy.2012.11.023.
[37] Sandia National Lab, "Hydrogen Engine," https://ecn.sandia.gov/engines/hydrogen-engine/. [Online]. Available: https://ecn.sandia.gov/engines/hydrogen-engine/.
[38] Thoo WJ, Kevric A, Ng HK, Gan S, Shayler P, La Rocca A. Characterisation of ignition delay period for a compression ignition engine operating on blended mixtures of diesel and gasoline. Appl Therm Eng May 2014;66(1–2):55–64. https://doi.org/10.1016/j.applthermaleng.2014.01.066.
[39] M. R. A. Mansor, S. Nakao, K. Nakagami, M. Shioji, and A. Kato, "Ignition characteristics of hydrogen jets in an argon-oxygen atmosphere," in *SAE Technical Papers*, SAE International, 2012. doi: 10.4271/2012-01-1312.
[40] Mansor MRA, Shioji M. Investigation of the combustion process of hydrogen jets under argon-circulated hydrogen-engine conditions. Combust Flame Nov. 2016;173:245–57. https://doi.org/10.1016/j.combustflame.2016.07.032.
[41] Peters M, Maes N, Dam N, van Oijen J. Characterizing and visualizing the direct injection of hydrogen into high-pressure argon and nitrogen environments. Int J Hydrogen Energy May 2024;66:304–15. https://doi.org/10.1016/j.ijhydene.2024.04.054.
[42] Bradley D, Kalghatgi GT. Influence of autoignition delay time characteristics of different fuels on pressure waves and knock in reciprocating engines. Combust Flame Dec. 2009;156(12):2307–18. https://doi.org/10.1016/j.combustflame.2009.08.003.
[43] Ksenia Siadkowska, "IHAPC project." Accessed: Jan. 11, 2026. [Online]. Available: https://sites.uwasa.fi/ihapc/.
[44] Şener R, Gül MZ. Optimization of the combustion chamber geometry and injection parameters on a light-duty diesel engine for emission minimization using multi-objective genetic algorithm. Fuel Nov. 2021;304. https://doi.org/10.1016/j.fuel.2021.121379.
[45] J. XU, X. JIANG, Y. WANG, N. DONG, L. QIAO, and J. BAI, "Progress in local-variable-based transition-turbulence models for subsonic and transonic boundary layers," *Chinese Journal of Aeronautics*, p. 103688, Apr. 2025, doi: 10.1016/j.cja.2025.103688.
[46] Wang B, et al. Optical and simulation investigation of effect of jet-wall interaction on combustion performance of methanol pre-chamber turbulent jet ignition system. Appl Energy May 2025;385. https://doi.org/10.1016/j.apenergy.2025.125533.